PNAS RESEARCH ARTICLE | NEUROSCIENCE ENGINEERING

# Mapping fast tissue dynamics with long camera exposures via intensity modulation

Hengfa Lu[a], Qingwei Fang[a], Jewel A. Ashbrook[a,b], Victoria Nemchek[c], Michela Fracassi[c], Theresa A. Jones[c], and Andrew K. Dunn[a,1]

Affiliations are included on p. 8.

Edited by David A. Weitz, Harvard University, Cambridge, MA; received October 15, 2025; accepted March 4, 2026

**Measuring fast dynamic processes with dynamic light scattering over wide fields of view is critical for applications ranging from blood flow imaging to characterizing complex fluids, yet is often limited by the need for expensive, high frame rate cameras. Here, we introduce sinusoidal intensity modulation speckle imaging (SIMSI), a technique that overcomes this hardware limitation by encoding information about fast dynamics into images captured with long camera exposures. Within each exposure, we sinusoidally modulate the illumination intensity, yielding frequency selective speckle variance measurements that sample the power spectral density (PSD) of intensity fluctuations. By sweeping the modulation frequency across exposures, SIMSI maps the PSD while preserving high signal-to-noise long exposures. We fit the measured spectra with a flexible model and report a spectral cutoff frequency $f_c$ as a flow index. In controlled flow microfluidic phantoms, SIMSI PSD estimates agree with the reference PSD measurements from a coaligned high-speed detector, and the derived $f_c$ varies linearly with the imposed flow velocity ($R^2 > 0.999$). In vivo in the mouse cortex, the SIMSI derived $f_c$ maps distinguish vascular compartments with distinct spectral signatures. Finally, SIMSI tracks the spatiotemporal evolution of cortical blood flow changes for ten days following ischemic stroke. SIMSI provides a robust and accessible method for wide field, frequency domain characterization of fast dynamics using standard cameras. This advance enables a richer characterization of complex systems and has wide ranging applications in biomedicine, engineering, and physics.**

cerebral blood flow imaging | laser speckle contrast imaging | light intensity modulation | power spectral density | dynamic light scattering

## Significance

Characterizing fast biological dynamics, such as blood flow in the brain's microvasculature, across wide fields is crucial but typically demands expensive, specialized high-speed cameras. We address this limitation with sinusoidal intensity modulation speckle imaging (SIMSI), which encodes rapid dynamics within a long camera exposure. By decoupling the effective measurement timescale from frame rate, SIMSI captures microsecond to millisecond dynamics using standard cameras. Sweeping the modulation frequency yields wide field maps of the fluctuation spectrum, enabling frequency-resolved characterization of tissue dynamics. We validate SIMSI measurements with a coaligned high-speed reference detector and demonstrate utility by tracking cerebrovascular changes for ten days after stroke. This accessible method for wide field spectral mapping opens avenues for studying disease, materials, and complex fluids.

Temporal intensity fluctuations arising from dynamic light scattering in biological tissue carry rich physiological and biophysical information, most notably microvascular blood flow, tissue perfusion, and particle diffusion, through the temporal intensity autocorrelation function $g_2(\tau)$ and its Fourier dual, the power spectral density (PSD) (1–3). In principle, wide-field imaging of these dynamics would allow quantitative mapping of perfusion and flow heterogeneity over large fields of view, enabling new insights in basic neuroscience, stroke and oncology monitoring, and intraoperative guidance (4–8). In practice, however, the decorrelation timescales of $g_2(\tau)$ range from microseconds to milliseconds, demanding sampling rates well beyond those of standard scientific cameras. Although high speed detectors can resolve these dynamics, they are constrained by cost, instrument complexity, or field of view.

To bridge this gap to direct temporal characterization, a diverse range of wide-field techniques has emerged. Hardware accelerated approaches pursue direct, fast sampling: dynamic light scattering imaging (DLSI) acquires pixelwise $g_2(\tau)$ using high frame rate cameras (9); large format single photon avalanche-diode (SPAD) arrays now integrate on chip autocorrelation for massively parallel diffuse correlation measurements (10, 11); and event-based neuromorphic sensors provide microsecond-latency readout for speckle dynamics (12). A complementary strategy uses camera architectures to reformat time into space, such as rolling shutter speckle imaging (RSSI), which exploits the row-wise readout of commodity CMOS sensors to recover temporal decorrelation in a single frame (13, 14).

An alternate strategy has been to develop computational methods that infer fast dynamics from time-integrated measurements made with standard cameras. This includes laser speckle contrast imaging (LSCI), multiexposure speckle imaging (MESI), and speckle contrast optical spectroscopy (SCOS), and related speckle visibility approaches (15–20). Recently, a time domain variant using pulsed intensity modulation has enabled wide-field mapping of quasi–$g_2(\tau)$ with ordinary cameras (21). Collectively, these

Competing interest statement: The University of Texas at Austin has filed a provisional patent application that covers part of the work on sinusoidal intensity modulation imaging covered in this paper; H.L. and A.K.D. are listed as inventors on the patent application.

This article is a PNAS Direct Submission.



[1]To whom correspondence may be addressed. Email: adunn@utexas.edu.

This article contains supporting information online at https://www.pnas.org/lookup/suppl/doi:10.1073/pnas.2524940123/-/DCSupplemental.

Published April 23, 2026.

advances extend temporal reach or interpretability, but they either demand specialized, high-throughput sensors (limiting cost and field of view) or rely on simplified models that reduce sensitivity to multiscale dynamics. Moreover, when photon budgets are tight, approaches that rely on very short integration windows (short exposures or low duty cycle pulsed illumination) can become photon-limited and degrade the precision of speckle-visibility statistics.

Here, we introduce sinusoidal intensity modulation speckle imaging (SIMSI), a frequency domain approach that overcomes these limitations by enabling measurement of rapid speckle dynamics with only standard, low frame rate cameras. The principle is to modulate the illumination intensity with a sinusoidal waveform at a chosen frequency, $f_m$, within a single, long camera exposure. We show that the speckle variance, $K^2(T, f_m)$, provides a frequency localized sample of the PSD of the intensity fluctuations at $f = f_m$. By sweeping the modulation frequency across successive frames, SIMSI builds the full PSD without requiring high frame rate acquisition or assuming a specific form of the PSD or $g_2(\tau)$. Crucially, the use of long integration times for each spectral point makes the measurement highly photon-efficient, a critical advantage for low-light imaging conditions. To characterize the measured PSD, we fit a flexible model, $\mathcal{P}(f) = a(1 + (f/f_c)^\gamma)^{-1} + b$, to extract flow-related maps (here, a spectral cutoff frequency $f_c$) for wide-field imaging. This work first validates SIMSI in controlled flow phantoms and healthy mouse cortex, and then applies it to track cerebrovascular changes following ischemic stroke. This advance provides an accessible and robust method for quantitative, wide-field analysis of dynamic systems with broad applications in biomedicine and materials science.

## Results

**Principle of SIMSI.** When coherent light scatters from dynamic media, such as biological tissue, it creates a random interference pattern known as speckle (15, 22). The temporal fluctuations of this pattern carry rich information about the motion of scatterers, such as blood cells. In LSCI, these dynamics are quantified by the speckle contrast, $K(T)$, which measures the degree of blurring over a camera exposure time $T$. The normalized speckle variance, $K^2(T)$, for a constant illumination is related to the sample's intensity autocorrelation function, $g_2(\tau)$, by

$$K^2(T) = \frac{2}{T^2}\int_0^T (T-\tau)g_2(\tau)d\tau - 1. \qquad [1]$$

Since $g_2(\tau)$ enters through an integral operator, recovering a compact decorrelation metric from $K^2(T)$ is generally not feasible without additional assumptions (e.g., a parametric family for $g_1(\tau)$ and additional terms such as static scattering and noise). While powerful, such assumptions can be challenged by heterogeneous, multiscale dynamics in living tissues and may be susceptible to model mismatch (23–25). Furthermore, the appropriate model form can vary within a single image (9).

To overcome this limitation, one can modulate the illumination intensity within the camera exposure. Our recent work (21) has shown that using short pulsed modulation can directly sample the time-domain intensity autocorrelation function, $g_2(\tau)$. However, this approach can be limited by low photon throughput due to the low duty cycle of the short pulses. Here, we introduce a fundamentally different approach by shifting the measurement from the time domain to the frequency domain. This is justified by the Wiener–Khinchin theorem, which states that for a stationary process the PSD, $\mathcal{P}_I(f)$, is the Fourier transform of the autocorrelation function and thus contains identical information about the dynamics. This shift to the frequency domain enables frequency-resolved measurements that can be used to map the PSD of the intensity fluctuations, and the continuous sinusoidal modulation improves photon efficiency.

As we show in a detailed derivation (*SI Appendix*, Note S1), applying a sinusoidal modulation $m(t) = \frac{1}{2} + \frac{1}{2}\cos(2\pi f_m t)$ (Fig 1) establishes a direct relationship between the measured speckle variance and the sample's PSD, $\mathcal{P}_I(f)$:

$$K^2(T, f_m) = \int_{-\infty}^{\infty} \mathcal{P}_I(f)\,\mathrm{sinc}^2(fT)df + \frac{1}{2}\int_{-\infty}^{\infty} \mathcal{P}_I(f)\,\mathrm{sinc}^2\left((f-f_m)T\right)df - 1. \qquad [2]$$

Here $\mathrm{sinc}(x) = \sin(\pi x)/(\pi x)$. Eq. **2** defines the SIMSI measurement operator: for fixed exposure $T$, each acquisition at modulation frequency $f_m$ yields a speckle-variance statistic $K^2(T, f_m)$ that is a known, frequency-localized (band-averaged) linear functional of the intensity-fluctuation PSD $\mathcal{P}_I(f)$, with an effective bandwidth on the order of $1/T$. Note that for fixed $T$, the first term is constant across $f_m$, while the second term shifts with $f_m$ and carries the spectral dependence used to map the PSD shape. By varying $f_m$, we can build up the shape of the PSD. The width of this weighting band, and thus the spectral resolution of the measurement, is inversely proportional to the camera exposure time, $T$.

To the best of our knowledge, no established model exists for the PSD of speckle fluctuations from blood flow. We therefore introduce a phenomenological model based on a modified Lorentzian function, $\mathcal{P}(f) = a(1 + (f/f_c)^\gamma)^{-1} + b$. In this model, the cutoff frequency $f_c$ serves as a flow-related spectral index under the stated geometry and optical conditions; $\gamma$ is the spectral exponent describing the steepness of the decay; $a$ is the amplitude of the dynamic signal; and $b$ is a static offset term. The validation and application of this framework are presented in the following sections.

**Quantitative Validation of SIMSI in Controlled Flow Phantoms.** To evaluate the performance of SIMSI, we imaged a microfluidic flow phantom containing a tissue-mimicking scattering solution with precisely controlled flow rates (corresponding to 0.0 to 10.4 mm/s), spanning physiological ranges. We first demonstrated the ability of SIMSI to map flow dynamics by generating maps of the fitted cutoff frequency, $f_c$. Representative $f_c$ maps, alongside their corresponding speckle contrast ($K$) maps, clearly distinguish the channel from the static background at both low (0.2 mm/s) and high (8.3 mm/s) flow velocities, with higher $f_c$ values corresponding to faster flow (Fig. 2*B*).

The core principle of SIMSI, its ability to accurately measure the PSD, was validated by comparing our measurements against a coaligned, high-speed SiPM reference (26, 27). Across a wide range of flow velocities, the normalized $K^2$ values measured by SIMSI at different modulation frequencies show excellent agreement with the reference PSD curves measured by the SiPM (Fig. 2*C*). This confirms that our method accurately samples the underlying dynamics.

Building on this, we confirmed the quantitative accuracy of our derived flow metric. The mean cutoff frequency, $\langle f_c \rangle$, extracted from the channel region of interest (ROI) exhibits a strong linear correlation ($R^2 > 0.999$) with the programmed flow

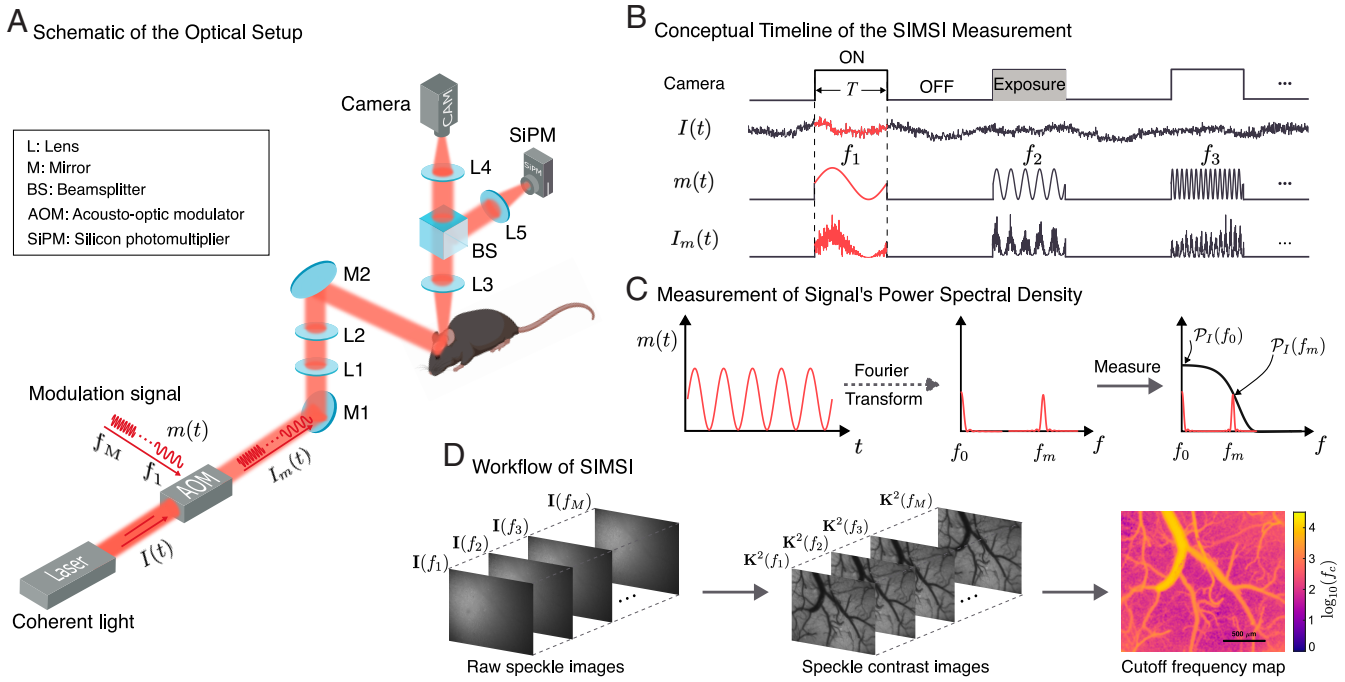


**Fig. 1.** Principle and implementation of SIMSI. (*A*) Simplified schematic of the optical setup. (*B*) Conceptual timeline of the SIMSI measurement principle. The rapidly fluctuating speckle intensity from the sample, $I(t)$, is modulated by a continuous sinusoidal waveform, $m(t)$, within a single camera exposure of duration $T$. This approach decouples the measurement of fast dynamics from the camera's acquisition speed. (*C*) The measurement process in the frequency domain. The measured speckle variance $K^2(T, f_m)$ provides a frequency-localized weighting of the underlying PSD, with an effective bandwidth set by $1/T$ through a $\mathrm{sinc}^2$ kernel. By varying $f_m$, the full shape of the PSD can be mapped. (*D*) Example workflow of SIMSI. A representative high-resolution map of the cutoff frequency ($f_c$), derived from SIMSI measurements of the mouse cerebral cortex, demonstrates the technique's ability to visualize the microvasculature.

velocity (Fig. 2*D*). Furthermore, SIMSI provides sufficient spatial resolution to resolve the characteristic parabolic flow profile within the microfluidic channel, as shown in the cross-sectional profiles of $f_c$ (Fig. 2 *E* and *F*). Together, these results validate SIMSI as a quantitative method for sampling the intensity-fluctuation PSD and for producing a repeatable flow-related spectral index under controlled phantom conditions. Direct experimental comparisons to conventional MESI (16) and 2P-MESI (21), including a photon-limited regime, are provided in *SI Appendix*, Note S3 and Figs. S3 and S4).

**High-Resolution Mapping of Cerebrovascular Dynamics in the Healthy Mouse Cortex.** Having validated SIMSI in controlled phantoms, we next sought to evaluate its performance for blood flow imaging in vivo. We performed wide-field imaging through a cranial window over the cortex of healthy mice (Fig. 3*A*). The resulting cutoff frequency ($f_c$) maps, generated from the SIMSI data, reveal the surface cortical vasculature with excellent detail. Different types of vessels are clearly resolved and distinguished from the surrounding parenchyma, which exhibits lower $f_c$ values (Fig. 3*B*).

To quantify these observations, we performed an ROI analysis on different vascular and tissue compartments. This analysis confirmed that SIMSI can quantitatively differentiate these regions, with ROIs placed on cortical vessels showing a significantly higher mean $f_c$ than those in the parenchyma, consistent with expected differences in flow-related dynamics between resolvable surface vessels and the surrounding parenchyma (Fig. 3*C*). Furthermore, we validated the accuracy of the underlying spectral measurement in vivo by comparing SIMSI data with measurements from a coaligned, high-speed SiPM. For ROIs placed on representative vessels, $K^2$ values measured by SIMSI align with the reference PSD curves acquired by the SiPM (Fig. 3*D*).

Finally, we assessed physiological consistency at vessel bifurcations via a conservation of flow analysis (Fig. 3*E*) (24, 28). Prior work in speckle-visibility imaging has shown that decorrelation rate indices derived from speckle (e.g., ICT) depend not only on red blood cell speed but also on caliber-dependent sensitivity, such that diameter scaling reduces systematic caliber effects for resolvable surface vessels in reflectance geometry (24). Under steady conditions, a diameter-scaled index is therefore expected to be conserved across a bifurcation (parent → daughters) as an empirical surrogate for flow conservation (28).

Motivated by this framework, we define a flow index $\mathrm{FI} = D\langle f_c \rangle$, where $D$ is the measured vessel diameter and $\langle f_c \rangle$ is the mean cutoff frequency within the vessel ROI. We then evaluate conservation across Y-shaped bifurcations ($\mathrm{FI}_P \approx \mathrm{FI}_{D1} + \mathrm{FI}_{D2}$; percent error defined in *Methods*). Across multiple bifurcations, the mean percent error was less than 5%, supporting $f_c$ as a robust, flow-related spectral index in vessels for mapping spatial heterogeneity and longitudinal change, without implying a universal conversion to absolute speed.

**Longitudinal Monitoring of Vascular Dynamics Following Ischemic Stroke.** To demonstrate the utility of SIMSI for tracking chronic blood flow dynamics, we applied it to a photothrombotic stroke model in the mouse cortex, monitoring cerebrovascular dynamics over a 10-d period alongside conventional MESI (16). We use MESI here as an established reference for longitudinal trend comparison. Following baseline imaging, we induced a targeted ischemic injury in a surface arteriole. We then imaged the subsequent evolution of blood flow dynamics at multiple time points postocclusion (Fig. 4).

A direct visual comparison of the time-series maps shows that SIMSI and MESI report broadly consistent spatial patterns and

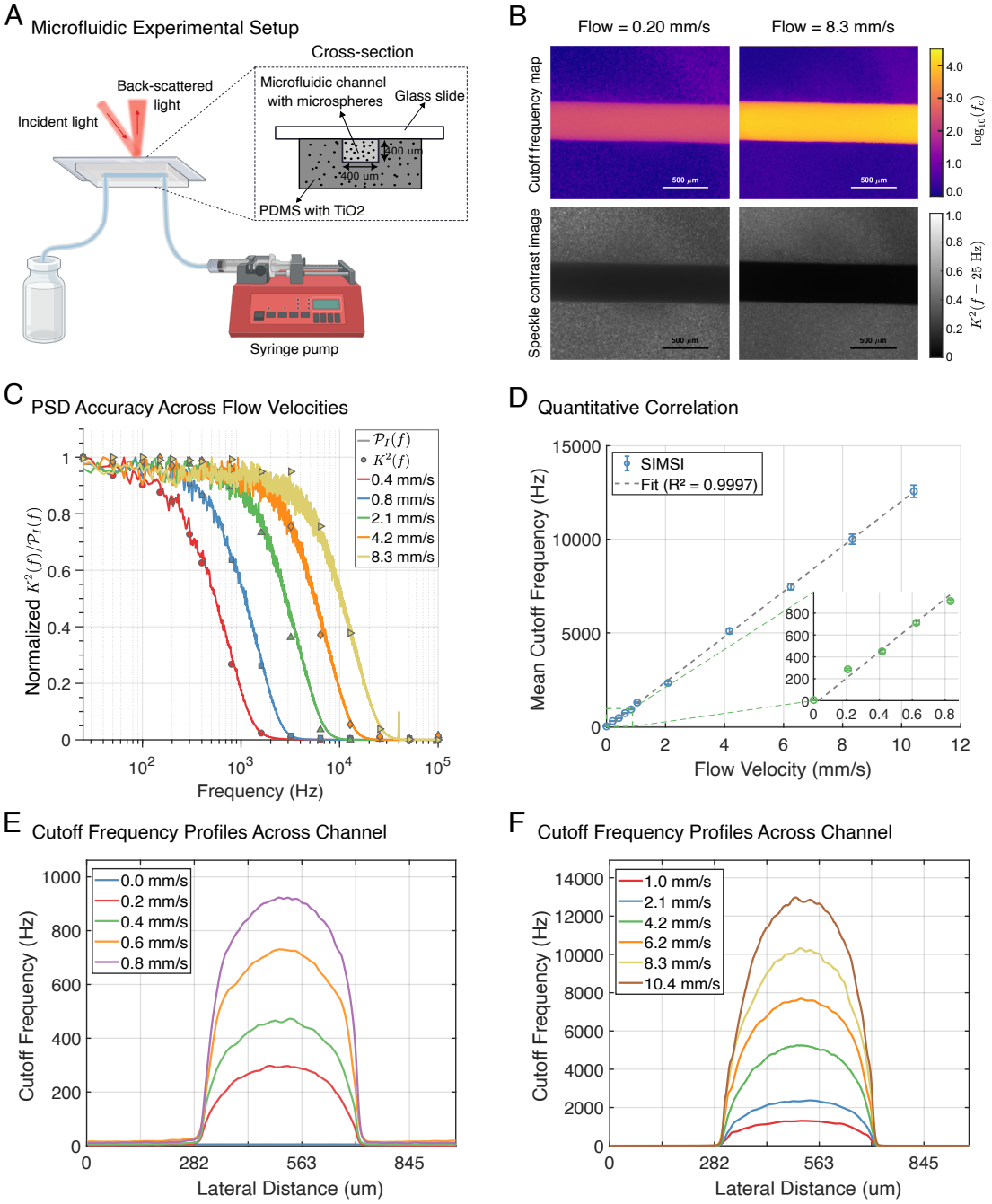


**Fig. 2.** Quantitative validation of SIMSI in a microfluidic flow phantom. (*A*) Microfluidic channel setup with tissue-mimicking scattering solution. (*B*) Representative speckle contrast ($K$) maps and the corresponding fitted cutoff frequency ($f_c$) maps at low (0.20 mm/s) and high (8.3 mm/s) flow velocities. (*C*) Comparison of SIMSI measurements to reference PSDs across five different flow speeds. Discrete data points (symbols) represent the normalized $K^2$ values measured by SIMSI, which show excellent agreement with the corresponding PSD curves (solid lines) measured by a reference detector. (*D*) Mean fitted $f_c$ from the channel ROI shows a strong linear correlation ($R^2 = 0.9997$) with the controlled flow velocity. Error bars represent the SD within the ROI. (*E* and *F*) Spatial cross-sectional profiles of $f_c$ resolve the parabolic flow profile within the channel.

recovery trajectories (Fig. 4*A*), while differing most strongly in the ischemic core immediately after occlusion. At day 1, the SIMSI cutoff frequency ($f_c$) maps indicate a pronounced ischemic core with markedly reduced perfusion. The inverse correlation time (ICT) maps from MESI also clearly identify the ischemic region, though the apparent suppression in the core is less extreme. During the chronic phase, the day-6 $f_c$ map qualitatively shows more recognizable microvascular features than the corresponding MESI map, whereas this difference is not apparent by day 10. This pattern is consistent with increased parenchymal perfusion near the infarct by day 10, which reduces vessel-parenchyma contrast for both methods.

We analyzed the temporal evolution of flow metrics within four distinct regions of interest (ROIs) (Fig. 4*B*). The SIMSI data (top subplot) show a larger dynamic range at day 1, with $f_c$ in both the ischemic core and the targeted artery shifting to values below 10 Hz. The MESI data (bottom subplot) track the same overall trends across ROIs and time points, but the ICT values in the ischemic core remain comparatively elevated. This divergence is expected in the very low-flow regime: for time-integrated

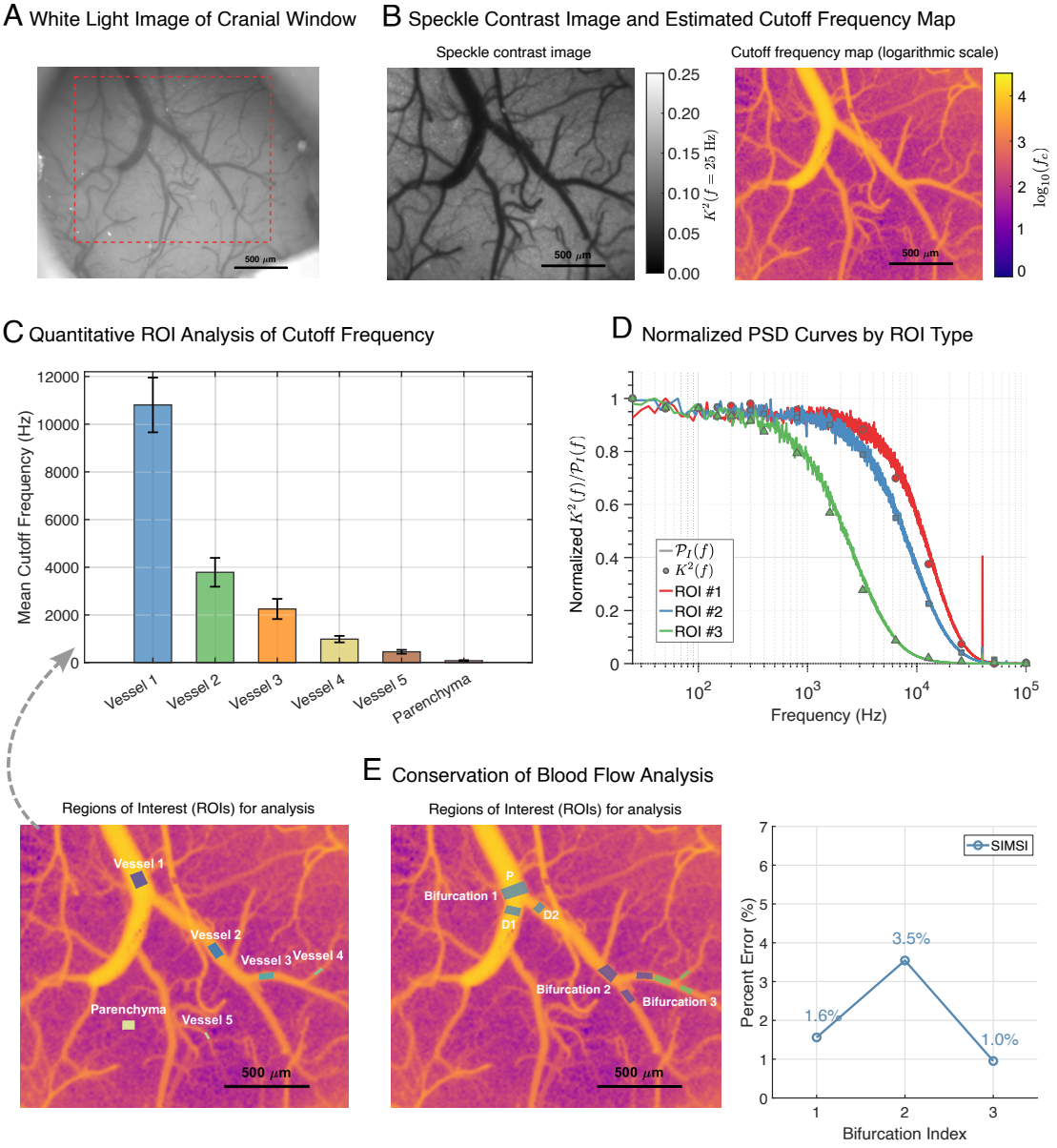


**Fig. 3.** High-resolution mapping and quantitative validation of cortical dynamics in a healthy mouse using SIMSI. (*A*) White light overview of the exposed cortical surface through a cranial window, with the region mapped by SIMSI indicated by the dashed box. (Scale bar, 500 μm.) (*B*) Representative maps from the indicated region: (*Left*) an averaged speckle contrast ($K$) image, and (*Right*) the corresponding fitted cutoff frequency ($f_c$) map. The $f_c$ map clearly delineates the microvasculature. (Scale bar, 500 $\mu$m.) (*C*) Quantitative differentiation of vascular features. An $f_c$ map with ROIs placed on representative vessels and parenchyma is shown (*Bottom*), with the corresponding mean $f_c$ values (*Top*) demonstrating statistically distinct dynamic signatures. (*D*) In vivo validation of the PSD measurement. Normalized $K^2$ values measured by SIMSI (symbols) from representative ROIs show excellent agreement with the reference PSD curves (solid lines) measured by a coaligned reference detector. (*E*) Physiological validation via conservation of flow. An $f_c$ map shows ROIs on a parent vessel (P) and its two daughter branches (D1, D2) (*Left*). The calculated flow index (FI $\propto$ Diameter $\times$ $f_c$) is conserved through the bifurcation, with the sum of daughter FIs matching the parent FI with low percent error across multiple analyzed bifurcations (*Right*).

speckle-variance measurements at feasible exposure times, changes in correlation time can produce only weak changes in $K^2(T)$, which limits sensitivity to near-stasis dynamics. In this context, the reduced low-flow sensitivity is a practical limitation, primarily when distinguishing near-zero flow from severely reduced flow is important; it does not change the qualitative conclusion that both methods capture partial reperfusion over the subsequent 10-d period.

We further analyzed pixel-value distributions within the ischemic core ROI at key time points (Fig. 4*C*). At baseline, both techniques show broad distributions consistent with heterogeneous flow contributions. At day 1, the SIMSI distribution collapses into a tight, bimodal distribution in the near-stasis regime (peaks at approximately 2 and 4 Hz), whereas the MESI distribution is confined to substantially higher values with a long tail, consistent with reduced sensitivity of time-integrated metrics in this regime. By day 10, SIMSI reveals a recovered distribution that is a single, narrow peak centered around 250 Hz, consistent with the parenchymal flow component of baseline, while the high-flow arterial component is absent—a pattern consistent with persistent occlusion and/or chronic vascular remodeling of the targeted vessel.

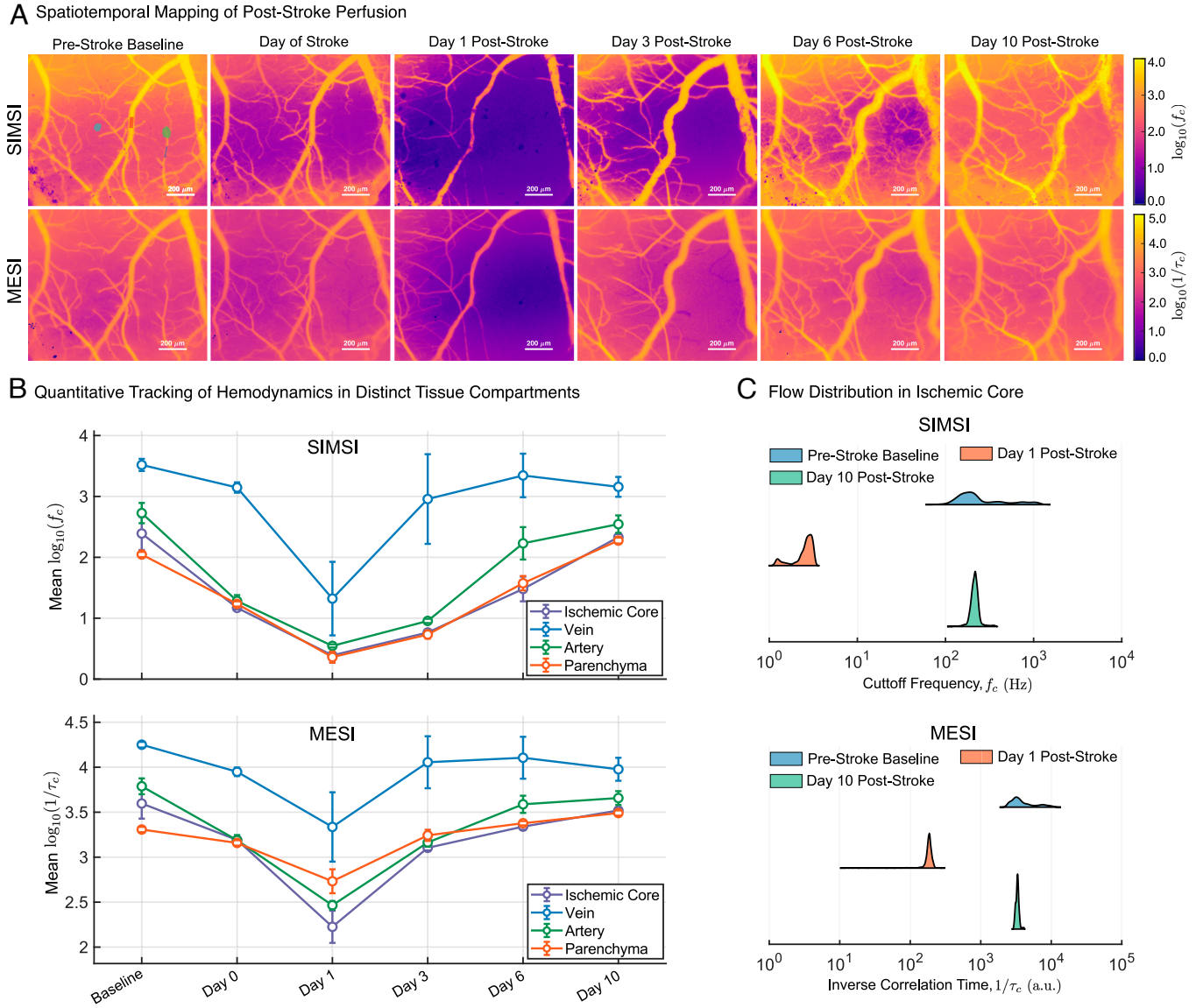


**Fig. 4.** SIMSI provides a high-fidelity longitudinal account of ischemic injury and recovery. (*A*) Representative flow maps from a mouse cortex imaged longitudinally before and after a photothrombotic stroke. The top row shows SIMSI maps of the cutoff frequency, $f_c$ (log scale), while the bottom row shows conventional MESI maps of the ICT (log scale). Both colormaps are fixed across all time points for fair comparison. Outlines of the four ROIs used for quantitative analysis are shown on the baseline SIMSI map. (*B*) Temporal evolution of mean flow metrics within the four ROIs. The top subplot displays the data from SIMSI, while the bottom subplot shows the corresponding data from conventional MESI. Error bars represent the SD of pixel values within each ROI. (*C*) Comparative distribution plots of pixel values within the Ischemic Core ROI at three key time points for SIMSI (*Up*) and conventional MESI (*Bottom*). The shape of each distribution represents the heterogeneity of flow within the region.

## Methods

**SIMSI Theory and Signal Processing.** SIMSI relates the measured speckle variance, $K^2(T, f_m)$, to the PSD of the detected intensity fluctuations, $\mathcal{P}_I(f)$, through a known frequency-domain measurement operator. For the sinusoidal modulation waveform $m(t) = \frac{1}{2} + \frac{1}{2}\cos(2\pi f_m t)$ and an exposure time $T$, the resulting relationship is (complete derivation in *SI Appendix*, Note S1):

$$K^2(T, f_m) = \int_{-\infty}^{\infty} \mathcal{P}_I(f)\ \mathrm{sinc}^2(fT)\, df + \frac{1}{2}\int_{-\infty}^{\infty} \mathcal{P}_I(f)\ \mathrm{sinc}^2\left((f - f_m)T\right) df - 1, \quad [3]$$

where $\mathrm{sinc}(x) = \sin(\pi x)/(\pi x)$. In all experiments, we chose $f_m$ such that $f_m T \in \mathbb{Z}$, under which the compact operator form in Eq. **3** holds (*SI Appendix*, Note S1).

We parameterize the PSD with a flexible phenomenological model, $\mathcal{P}(f) = a\left(1 + (f/f_c)^{\gamma}\right)^{-1} + b$, and report the cutoff frequency $f_c$ as a flow-related spectral index. For each pixel, the set of measurements $\{K^2(T, f_{m,\ell})\}_{\ell=1}^{L}$ was fit using a physics-informed, data-driven estimator; implementation details and constraints are provided in *SI Appendix*, Note S2.

**Optical Setup.** The primary SIMSI system was designed for validation and high-resolution mapping. A 785 nm laser diode (L785P090, Thorlabs) served as the coherent light source. The beam was collimated before entering an acousto-optic modulator (AOM, AOMO 3100-125, Gooch & Housego), which modulated the laser intensity. The modulated beam was then directed to the imaging target. Backscattered light from the sample was collected by a camera lens (AF NIKKOR 24 mm f/2.8D, Nikon) and split by a 50:50 beamsplitter (BSW17, Thorlabs). The transmitted arm (beamsplitter output) was focused by a second lens (AF NIKKOR 50 mm f/1.8D, Nikon) onto a camera (acA1920-155 um, Basler). The reflected light was focused onto a fiber-coupled (P3-780A-

FC-2, Thorlabs) silicon photomultiplier (SiPM) (27) for coaligned, reference measurements. The SiPM signal was filtered (500 kHz; EF506, Thorlabs) and sampled at 1 MHz by a data acquisition board (USB-6363, National Instruments). The camera was operated in 8-bit mode for all measurements. The AOM was driven with sinusoidal modulation frequencies matched to the exposure time to satisfy the integer-cycle condition ($f_m T \in \mathbb{Z}$).

For the photothrombotic stroke induction (29) and subsequent longitudinal imaging, the optical path was modified. The 50:50 beamsplitter and the SiPM branch were replaced with a dichroic mirror to introduce a focused 520 nm green laser beam (L520A2, 110 mW, Thorlabs) coaligned with the imaging axis. For these sessions, a 5X Mitutoyo Plan Apo Infinity Corrected Long WD Objective was used.

**Microfluidic Flow Phantom Experiments.** To quantitatively validate SIMSI under controlled conditions, a microfluidic phantom was designed to simulate blood flow in a simplified tissue environment. A single-channel microfluidics device was fabricated from polydimethylsiloxane (PDMS) mixed with 1.8% w/w titanium dioxide. This mixture was chosen to create a bulk medium with optical properties mimicking those of biological tissue (30). The scattering solution flowing through the channel was prepared by diluting 1 $\mu$m latex microspheres (5100A, 10% w/w, Thermo Fisher Scientific) to a 4.8% v/v ratio with distilled water to mimic the scattering properties of blood. This solution was driven through the channel at controlled flow rates ranging from 0.0 to 10.4 mm/s using a syringe pump (ALADDIN-100, World Precision Instruments), corresponding to the physiological range of cerebral blood flow speeds.

**Animal Subjects and Surgical Procedures.** All animal procedures were approved by the Institutional Animal Care and Use Committee (IACUC) of the University of Texas at Austin. Experiments were performed on adult C57BL-6 mice. Mice were anesthetized with 3% isoflurane in oxygen delivered via a nose cone. During all surgical and imaging procedures, body temperature was maintained at 37 °C with a feedback-controlled heating system (Harvard Apparatus Homeothermic Monitoring System). During surgery, they received carprofen (10 mg/kg) and dexamethasone (0.2 mg/kg). Every 24 h for the first 72 h postsurgery, they received carprofen (10 mg/kg).

For the surgical procedure, the mouse's head was fixed to a stereotaxic frame (Narishige). After resecting the scalp to expose the skull, a 4-mm diameter craniotomy was performed over the motor cortex using a dental drill. A 4-mm round glass coverslip (#1.5, World Precision Instruments) was placed over the exposed brain, and dental cement was applied to the perimeter to create an airtight seal between the coverslip and the skull. A final layer of cyanoacrylate was applied over the cement to fill any porous regions and ensure a durable, sealed cranial window. Animals were allowed to recover fully from anesthesia and were monitored for normal behavior before the first imaging session.

**Imaging and Experimental Protocols.** For all SIMSI experiments, data were acquired at a set of modulation frequencies ($f_m$) spanning 25 to 100 kHz (25, 50, 100, 150, 200, 300, 400, 800, 1,600, 3,200, 6,400, 12,800, 25,600, 51,200, and 100,000 Hz). All modulation frequencies were selected such that $f_m T$ was an integer number of cycles for $T = 40$ ms. The camera exposure was set to 40 ms for each frequency, and 150 raw speckle images were acquired per setting. For the phantom validation studies, this acquisition sequence was repeated five times for each flow rate. Simultaneously, 80 seconds of reference data was recorded with the coaligned SiPM for direct comparison.

All in vivo experiments were conducted on anesthetized mice with implanted cranial windows. For baseline measurements and validation in the healthy cortex, data were collected from representative locations, with the full SIMSI and SiPM acquisition sequence repeated 5 times at each location.

A photothrombotic stroke was induced by intraperitoneal injection of Rose Bengal (15 mg/mL, 0.2 mL). After a 3-min interval, a 520-nm laser (20 mW; 0.3 mm beam diameter) was focused on a target descending arteriole to induce thrombosis. Longitudinal imaging was then performed at baseline (prestroke) and on days 0, 1, 3, 6, and 10 poststroke to track the full time-course of injury and recovery.

**Data and Statistical Analysis.** Spatial speckle contrast, $K$, was computed from raw images using a $7 \times 7$ sliding window, and speckle variance was computed as $K^2$. Parameter estimation for SIMSI used a physics-informed, data-driven fitting approach that enforces consistency with the corresponding forward model; details are provided in *SI Appendix*, Note S2. We interpret $f_c$ as a repeatable, flow-related spectral parameter under the stated optical geometry rather than as a calibration-free absolute speed measurement across conditions. ROIs for quantitative analyses were manually drawn over vessels and parenchymal regions.

For the conservation of flow analysis (24), vessel diameters were determined from the fitted $f_c$ map using a semiautomated method. First, a line segment was manually drawn perpendicular to the axis of the vessel of interest. An algorithm then automatically extracted multiple parallel intensity profiles centered on and adjacent to this line. These profiles were averaged to generate a single, high-SNR cross-sectional intensity profile of the vessel. This averaged profile was fitted to a Gaussian function, and the vessel diameter was defined as the full width at half maximum (FWHM) of the resulting Gaussian fit.

The flow index (FI) was calculated as $\mathrm{FI} = \text{Diameter} \times \langle f_c \rangle$, where $\langle f_c \rangle$ is the mean $f_c$ within the vessel ROI (24). For bifurcation analysis, the flow indices for the parent and two daughter vessels are denoted as $\mathrm{FI}_P$, $\mathrm{FI}_{D1}$, and $\mathrm{FI}_{D2}$, respectively. The percent error was calculated as $|\mathrm{FI}_P - (\mathrm{FI}_{D1} + \mathrm{FI}_{D2})|/\mathrm{FI}_P \times 100\%$.

This analysis follows prior speckle-visibility work in which diameter-scaled decorrelation rate indices are used as empirical flow conservation surrogates at bifurcations for resolvable surface vessels in reflectance geometry (24, 28).

## Discussions and Conclusions

In this work, we developed and validated SIMSI, a method that enables wide-field imaging of the PSD of fast tissue dynamics using only standard, low frame rate cameras. We have demonstrated that this technique is quantitatively accurate through validation in controlled flow phantoms against a high-speed reference detector. Furthermore, we have shown its utility for high-resolution in vivo mapping, successfully differentiating vascular compartments in the healthy mouse cortex based on their dynamic signatures. Finally, we applied SIMSI to track cerebrovascular changes longitudinally following ischemic stroke, highlighting its potential for studying disease pathophysiology.

The central technical contribution of SIMSI is a within-exposure encoding strategy that converts camera based speckle-visibility measurements into frequency localized sampling of the intensity-fluctuation PSD. Under sinusoidal modulation and the integer-cycle condition used throughout this work, each acquisition at modulation frequency $f_m$ yields a speckle-variance statistic $\widehat{K^2}(T, f_m)$ corresponding to a known, narrowband weighting of $\mathcal{P}_I(f)$ centered near $f_m$, with spectral resolution on the order of $1/T$. Varying $f_m$ therefore constructs a frequency-domain representation while retaining photon-efficient long exposures. By contrast, established speckle-visibility approaches (LSCI/MESI/SVS) operate under constant illumination and infer dynamics from how $K^2$ varies with exposure time $T$.

This shift in measurement operator also clarifies what is measured vs. what is inferred. SIMSI first acquires frequency-localized PSD samples determined by $(T, f_m)$; a compact descriptor is then obtained by postprocessing. Here, we parameterize the sampled PSD with a phenomenological model and report its cutoff frequency $f_c$ as a flow-related spectral index. Accordingly, $f_c$ is interpreted as a PSD-derived parameter whose relationship to flow speed is validated empirically under the stated optical conditions, rather than as a universal, calibration free conversion to absolute velocity.

Beyond enabling direct PSD sampling, SIMSI offers a practical advantage under photon-limited conditions. Because SIMSI acquires all frequency points with the same exposure time $T$ and comparable mean irradiance, the uncertainty of $\widehat{K^2}(T, f_m)$ is approximately uniform across $f_m$, which simplifies weighting

and stabilizes PSD fitting. More importantly, the sinusoidal waveform maintains a high within-exposure duty cycle, allowing long, photon-efficient integrations while placing sensitivity at selected fluctuation frequencies through the choice of $f_m$. This is especially important in the photon-limited regime: in the matched microfluidic-phantom comparisons (*SI Appendix*, Note S3 and Figs. S3 and S4), conventional MESI and 2P-MESI (21) did not return valid speckle-visibility statistics under a fixed peak-irradiance constraint without increasing the effective photon budget (e.g., higher peak power, additional averaging, or substantial binning), whereas SIMSI remained well-posed and continued to provide stable PSD measurements and $f_c$ over the full flow range.

As with other speckle-visibility methods, SIMSI relies on two practical assumptions: the detected field forms fully developed speckle and the underlying dynamics are approximately stationary over the acquisition used to estimate $\widehat{K^2}$. The sinusoidal modulation changes how dynamics are encoded within an exposure, but it does not alter photon transport; consequently, the sampling volume and effective probing depth are governed by the same factors as LSCI/MESI/SVS, namely the tissue optical properties, illumination/detection geometry, and imaging optics. For the wide-field reflectance configuration used here, SIMSI is therefore most sensitive to superficial cortical dynamics within the penetration range expected for conventional speckle contrast measurements, and the mapping between PSD-derived parameters (including $f_c$) and absolute speed should not be assumed to transfer across different media or geometries without calibration and validation. Likewise, in scattering regimes that deviate substantially from the multiply scattered conditions typical of cortical reflectance imaging (e.g., approaching a single-scattering limit), the PSD can remain well-defined but its interpretation and any mapping to scatterer motion require a regime-specific forward model. Finally, although we emphasize $f_c$ for interpretability, the full parameter set $(a, b, \gamma, f_c)$ is estimated jointly under explicit constraints (*SI Appendix*, Note S2), which mitigates parameter tradeoffs (e.g., between $\gamma$ and $f_c$) and supports stable spatial mapping.

Our longitudinal stroke model demonstrates SIMSI's ability to provide sensitive mapping of cerebrovascular pathophysiology. The enhanced sensitivity is particularly evident in low flow areas surrounding the ischemic core. The measurement of the PSD allows SIMSI to avoid the measurement saturation that can occur in time domain analysis as flow becomes pathologically slow. The result is a more accurate quantification of severe ischemia, as seen in the significant reduction of the $f_c$ signal in the ischemic core (Fig. 4 *B* and *C*). This finding has significant implications, suggesting that the severity of ischemic injury in preclinical models may be more profound than predicted by conventional techniques.

Furthermore, the distributional analysis provides deeper insight into the chronic recovery phase. While both methods show a return toward baseline flow by Day 10, the SIMSI data reveal a change in the underlying tissue composition (Fig. 4*C*). The recovered Day 10 distribution is a single, unimodal peak centered at a value consistent with healthy parenchymal flow. By comparing this to the heterogeneous baseline distribution, it is clear that the high-flow arterial signature has vanished. This provides a direct, quantitative signature of chronic vascular remodeling, likely indicating a persistent occlusion of the targeted vessel. This ability to quantitatively characterize changes in the composition of flow populations, and thus provide specific insights into neurovascular plasticity, is a key advantage of SIMSI's direct PSD measurement.

A related consideration for speckle-based blood flow measurements is physiological nonstationarity within an exposure. Our use of a relatively long exposure time, e.g., 40 ms, integrates over fast physiological oscillations like the cardiac cycle (which has a period of ~100 ms in mice). Therefore, the $f_c$ measured in the highly pulsatile vessels should be interpreted as not an instantaneous speed, but as a robust, time-averaged index of dynamic activity over the exposure window. For the applications demonstrated here, such as comparing vessel types and tracking chronic changes over hours and days poststroke, this time-averaged metric is highly effective and valid.

The SIMSI framework is also adaptable. Shorter exposure times (e.g., 5 to 20 ms) could reduce averaging over physiological oscillations, at the cost of reduced SNR per frame, and alternative modulation/encoding strategies could be used to trade acquisition time for decoding complexity. This work, focusing on PSD measurement, complements our prior approach (21) that uses pulsed modulation to sample the time-domain autocorrelation function $g_2(\tau)$. More broadly, the ability to map the PSD motivates future studies of whether disease or intervention alters not only overall flow level but also spectral structure, potentially providing contrast mechanisms beyond conventional speckle-contrast imaging.

In conclusion, SIMSI decouples the dynamics-encoding timescale from the camera acquisition rate and enables wide-field PSD mapping with accessible hardware. By providing a practical route to frequency-domain characterization of fast dynamics under standard-camera constraints, SIMSI makes characterization of complex dynamic systems practical for a broad range of scientific and engineering disciplines.

**Data, Materials, and Software Availability.** Representative processed data and MATLAB scripts have been deposited in Zenodo and are publicly available at https://doi.org/10.5281/zenodo.19210840 (31). All other data are included in the article and/or *SI Appendix*.

**ACKNOWLEDGMENTS.** We are grateful for funding from the following sources: the University of Texas at Austin (UT Austin Portugal Program) and NIH (NS108484). We thank Michael Giacomelli for helpful discussions about the SiPM detector.

Author affiliations: [a]Department of Biomedical Engineering, University of Texas at Austin, Austin, TX 78712; [b]Department of Physics, University of Texas at Austin, Austin, TX 78712; and [c]Psychology Department and Institute for Neuroscience, University of Texas at Austin, Austin, TX 78712

Author contributions: H.L. and A.K.D. designed research; H.L. and Q.F. performed research; H.L., J.A.A., V.N., M.F., and T.A.J. contributed new reagents/analytic tools; H.L. analyzed data; A.K.D. supervised the project; and H.L. and A.K.D. wrote the paper.

1. R. Bonner, R. Nossal, Model for laser Doppler measurements of blood flow in tissue. *Appl. Opt.* **20**, 2097–2107 (1981).
2. B. J. Berne, R. Pecora, *Dynamic Light Scattering: With Applications to Chemistry, Biology, and Physics* (Courier Corporation, 2000).
3. D. A. Boas, A. G. Yodh, Spatially varying dynamical properties of turbid media probed with diffusing temporal light correlation. *J. Opt. Soc. Am. A* **14**, 192–215 (1997).
4. U. Dirnagl, C. Iadecola, M. A. Moskowitz, Pathobiology of ischaemic stroke: An integrated view. *Trends Neurosci.* **22**, 391–397 (1999).
5. M. Czosnyka, P. Smielewski, S. Piechnik, L. A. Steiner, J. D. Pickard, Cerebral autoregulation following head injury. *J. Neurosurg.* **95**, 756–763 (2001).
6. C. Iadecola, Neurovascular regulation in the normal brain and in Alzheimer's disease. *Nat. Rev. Neurosci.* **5**, 347–360 (2004).
7. B. V. Zlokovic, Neurovascular pathways to neurodegeneration in Alzheimer's disease and other disorders. *Nat. Rev. Neurosci.* **12**, 723–738 (2011).
8. L. V. Wang, S. Hu, Photoacoustic tomography: In vivo imaging from organelles to organs. *Science* **335**, 1458–1462 (2012).
9. D. D. Postnov, J. Tang, S. E. Erdener, K. Kılıç, D. A. Boas, Dynamic light scattering imaging. *Sci. Adv.* **6**, eabc4628 (2020).
10. A. C. Ulku *et al.*, A 512 × 512 SPAD image sensor with integrated gating for widefield FLIM. *IEEE J. Quant. Electron.* **25**, 1–12 (2018).

11. A. Gorman *et al*., Atlas: A large array, on-chip compute SPAD camera for multispeckle diffuse correlation spectroscopy. *Biomed. Opt. Express.* **15**, 6499–6515 (2024).
12. Z. Ge, Y. Gao, H. K. H. So, E. Y. Lam, Event-based laser speckle correlation for micro motion estimation. *Opt. Lett.* **46**, 3885–3888 (2021).
13. C. Yi *et al*., Single-shot temporal speckle correlation imaging using rolling shutter image sensors. *Optica* **9**, 1227–1237 (2022).
14. C. Yi, S. Byun, Y. Lee, S. A. Lee, Improvements and validation of a spatiotemporal speckle correlation model for rolling shutter speckle imaging. *Biomed. Opt. Express.* **15**, 1253–1267 (2024).
15. A. K. Dunn, H. Bolay, M. A. Moskowitz, D. A. Boas, Dynamic imaging of cerebral blood flow using laser speckle. *J. Cereb. Blood Flow Metab.* **21**, 195–201 (2001).
16. A. B. Parthasarathy, W. J. Tom, A. Gopal, X. Zhang, A. K. Dunn, Robust flow measurement with multi-exposure speckle imaging. *Opt. Express* **16**, 1975–1989 (2008).
17. A. K. Dunn, Laser speckle contrast imaging of cerebral blood flow. *Ann. Biomed. Eng.* **40**, 367–377 (2012).
18. C. P. Valdes *et al*., Speckle contrast optical spectroscopy, a non-invasive, diffuse optical method for measuring microvascular blood flow in tissue. *Biomed. Opt. Express.* **5**, 2769–2784 (2014).
19. F. Fathi *et al*., Time-resolved laser speckle contrast imaging (TR-LSCI) of cerebral blood flow. *IEEE Trans. Med. Imaging* **44**, 1206–1217 (2025).
20. P. K. Dixon, D. J. Durian, Speckle visibility spectroscopy and variable granular fluidization. *Phys. Rev. Lett.* **90**, 184302 (2003).
21. Q. Fang, A. Tomar, A. K. Dunn, Wide-field intensity fluctuation imaging. *Biomed. Opt. Express* **15**, 1004–1020 (2024).
22. J. D. Briers, S. Webster, Laser speckle contrast analysis (LASCA): A nonscanning, full-field technique for monitoring capillary blood flow. *J. Biomed. Opt.* **1**, 174–179 (1996).
23. D. A. Boas, A. K. Dunn, Laser speckle contrast imaging in biomedical optics. *J. Biomed. Opt.* **15**, 011109 (2010).
24. S. M. S. Kazmi *et al*., Flux or speed? Examining speckle contrast imaging of vascular flows. *Biomed. Opt. Express* **6**, 2588–2608 (2015).
25. C. Liu, K. Kılıç, S. E. Erdener, D. A. Boas, D. D. Postnov, Choosing a model for laser speckle contrast imaging. *Biomed. Opt. Express.* **12**, 3571–3583 (2021).
26. S. M. S. Kazmi, R. K. Wu, A. K. Dunn, Evaluating multi-exposure speckle imaging estimates of absolute autocorrelation times. *Opt. Lett.* **40**, 3643–3646 (2015).
27. V. D. Ching-Roa, E. M. Olson, S. F. Ibrahim, R. Torres, M. G. Giacomelli, Ultrahigh-speed point scanning two-photon microscopy using high dynamic range silicon photomultipliers. *Sci. Rep.* **11**, 5248 (2021).
28. L. M. Richards *et al*., Intraoperative multi-exposure speckle imaging of cerebral blood flow. *J. Cereb. Blood Flow Metab.* **37**, 3097–3109 (2017).
29. T. A. Clark *et al*., Artery targeted photothrombosis widens the vascular penumbra, instigates peri-infarct neovascularization and models forelimb impairments. *Sci. Rep.* **9**, 2323 (2019).
30. C. T. Sullender *et al*., Using pressure-driven flow systems to evaluate laser speckle contrast imaging. *J. Biomed. Opt.* **28**, 036003 (2023).
31. H. Lu *et al*., Mapping fast tissue dynamics with long camera exposures via intensity modulation. Zenodo. https://doi.org/10.5281/zenodo.19210840. Deposited 24 March 2026.